A computationally efficient approach for soot modeling with discrete sectional method and FGM chemistry

Combustion and Flame 255 (2023) 112868

Contents lists available at ScienceDirect

Combustion and Flame

journal homepage: www.elsevier.com/locate/combustflame

A computationally efficient approach for soot modeling with discrete sectional method and FGM chemistry

Abhijit Kalbhor[a,*], Daniel Mira[b], Jeroen van Oijen[a,c]

[a] Department of Mechanical Engineering, Eindhoven University of Technology, Eindhoven, 5600 MB, the Netherlands
[b] Barcelona Supercomputing Center (BSC), Plaça Eusebi Güell, 1-3, Barcelona, 08034, Spain
[c] Eindhoven Institute for Renewable Energy Systems (EIRES), Eindhoven, 5600 MB, the Netherlands

ARTICLE INFO

Article history:
Received 19 May 2022
Revised 11 May 2023
Accepted 25 May 2023

Keywords:
Flamelet generated manifold
Discrete sectional methods
Soot formation

ABSTRACT

A novel approach for the prediction of soot formation in combustion simulations within the framework of discrete sectional method (DSM) based univariate soot model and Flamelet Generated Manifold (FGM) chemistry, referred to as FGM-CDSM, is proposed in this study. The FGM-CDSM considers the clustering of soot sections derived from the original soot particle size distribution function (PSDF) to minimize the computational cost. Unlike conventional DSM, in FGM-CDSM, governing equations for soot mass fractions are solved for the clusters, by using a pre-computed lookup table with tabulated soot source terms from the flamelet manifold, while the original soot PSDF is re-constructed in a post-processing stage. The flamelets employed for the manifold are computed with detailed chemistry and the complete sectional soot model. A comparative assessment of FGM-CDSM is conducted in laminar diffusion flames for its accuracy and computational performance against the detailed kinetics-based classical sectional model. Numerical results reveal that the FGM-CDSM can favorably reproduce the global soot quantities and capture their dynamic response predicted by detailed kinetics with a good qualitative agreement. Furthermore, compared to detailed kinetics, FGM-CDSM is shown to substantially reduce the computational cost of the complete reacting flow simulation with soot particle transport. Primarily, the use of FGM reduces the overall calculation by about two orders of magnitude compared to detailed kinetics, which is advanced further with the clustering of sections at a low memory footprint. Therefore, the present work demonstrates the promising capabilities of FGM-CDSM in the context of computationally efficient soot calculations and provides an excellent framework for extending its application to the simulations of turbulent sooting flames.

1. Introduction

In view of the detrimental impact of soot on the environment and health, legislative regulations concerning the amount and particle sizes of their emissions through practical combustion devices have become stringent in recent years. Consequently, to facilitate the accurate description of the dynamics of soot particles and the evolution of their size distributions, the role of detailed models predicting soot formation has become pivotal. The state-of-the-art methodologies for detailed soot modeling primarily include discrete sectional methods [1–4], method of moments (MOM) [5–7], and stochastic methods such as Monte Carlo (MC) [8,9]. MC-based models are computationally expensive and therefore limited to canonical 0-D and 1-D configurations. For multi-dimensional simulations, MOM-based soot models, which can adequately describe soot morphology at a low computational cost, are often employed [10,11]. However, the re-construction of PSDF with MOM approaches necessitates closure models for unsolved higher-order moments, which increases their mathematical complexity. On the other hand, DSM-based soot models enable a discretized representation of the soot PSDF in the particles' volume/mass space. Hence, a complete (discretized) PSDF can be accurately reproduced through the transport of soot scalars (mass fraction/number density) for each representative particle size (section). However, DSM-based models require a large number of sections (typically ranging from 30 to 100) to resolve the soot PSDF adequately, which makes them computationally demanding for multi-dimensional calculations. In general, a large number of chemical species and reactions need to be included in the kinetic mechanism to describe the evolution of gaseous phase soot precursors. Hence soot modeling with

* Corresponding author.
E-mail address: a.j.kalbhor@tue.nl (A. Kalbhor).

https://doi.org/10.1016/j.combustflame.2023.112868

detailed kinetics becomes very expensive, and its application in multi-dimensional simulations is rather impractical.

In the context of computational efficient combustion simulations with detailed chemistry, analytically-reduced, optimized kinetic schemes along with systematic automation are attractive. However, the solution of the soot phase remains an additional computational challenge, that supersedes the reduction achieved in the gas-phase description. Despite the progress in multicore architectures and CPU accelerators, the application of such reduced-order kinetic schemes becomes unaffordable for conditions of potential interest [12]. New machine-learning-based models [13] and virtual chemistry [12] techniques have been recently proposed for soot formation prediction in laminar and turbulent flames. While these methods were able to predict the first moments of the distribution (soot volume fraction and number density), the evolution of the soot particle size distribution was not examined. On the other hand, flamelet-based models are popular and often employed in multi-dimensional sooting flame simulations, to efficiently represent the combustion chemistry. In particular, tabulated chemistry coupled with MOM-based models has been widely applied in simulations of sooting flames [10,14]. Owing to the limitations of MOM-based models in capturing the soot PSDs, there have been efforts in integrating DSM-based soot models with tabulated chemistry within the RANS [15] and LES [3] frameworks. However, in the DSM-based simulations, although a significant reduction in CPU time can be achieved by employing flamelet-based tabulated chemistry, a large number of additional transport equations with the corresponding soot source terms integration are still required to represent the soot PSDF. In consequence, the reduction in CPU time achieved by the use of tabulated chemistry is lost if a large number of sectional transport equations are to be solved. Hence, for an effective application of DSM-based models in large-scale simulations, it becomes critical to develop computationally efficient approaches that can facilitate remarkable reductions in CPU time with minimum compromise on accuracy.

Different subprocesses associated with soot formation involve non-linear correlations between the gas-phase thermo-chemical states and soot variables. Hence, while coupling sectional models with tabulated chemistry, the dependence of soot source terms on the sectional soot variables is often explicitly accounted for during CFD calculation. Owing to the physical consistency regarding soot source term computation and the overall accuracy of soot prediction, computation of soot reaction rates is prevalent in the literature [3,15]. The performance of such a method in connection to FGM chemistry is also studied in our earlier work [16]. In the method relying on run-time computation of soot reaction rates, however, the CPU speedup is mainly due to the reduction of gas-phase kinetics, as soot source term calculation remains computationally intensive. On the other hand, the tabulation of soot reaction rates in flamelet-based models has been investigated in earlier works [17,18] for semi-empirical soot models. Additionally, the tabulated soot chemistry approach has recently been applied in simulations of turbulent spray flames [19], where the model was shown to effectively capture experimental trends. In the complete tabulation of soot reaction rates, the non-linear dependence of soot source terms on local soot variables is neglected, and soot formation is assumed to follow the characteristics of flamelets. Although the tabulation of soot source terms presents limitations in terms of the accuracy of soot prediction, it offers an interesting approach to reduce the computational cost for sooting flame calculations.

In this context, a new approach of coupling the DSM-based soot model with FGM tabulated chemistry [16], referred to as FGM-CDSM (Clustered-DSM), is proposed in this study to reduce the computational cost (CPU time, memory use) of tabulated source term based sectional soot modeling approaches. The rationale behind the FGM-CDSM model is to take one step further and assess if the complete tabulation of source terms followed by clustering of soot sections can yield reasonable results in terms of the prediction of global soot quantities, and evolution of soot PSD. This approach essentially considers a low dimensional representation of the soot PSDF by employing clustering of sections during simulation run-time, and a re-construction of the detailed PSDF in a post-processing stage based on PSDFs from the laminar flamelets. The proposed FGM-CDSM offers a good balance between accuracy and computational cost, as only a few transport equations are to be solved, making this model highly suitable for large-eddy simulations.

In the present work, the FGM-CDSM is first introduced and the clustering of soot sections is explained, followed by the assessment of its performance concerning the accuracy of soot prediction in laminar diffusion flames under steady, and unsteady conditions. In this assessment, first, we validate the FGM-CDSM approach against numerical results for global soot quantities (volume fraction, number density) and PSDs using the detailed model and with source term tabulation, but without clustering. Subsequently, global soot characteristics predicted by FGM-CDSM with clustering are compared against their no-clustering counterparts for a series of non-premixed ethylene flames. Here we primarily focus on investigating the capabilities of the proposed FGM-CDSM strategy in capturing soot formation characteristics and identifying possible deficiencies associated with its application to more general conditions. The present study is, therefore, limited to laminar flame simulations, as soot prediction in turbulent conditions presents additional challenges related to the closure of soot-turbulence-chemistry interactions and the sensitivity of the results to different models employed. Nevertheless, the selected unsteady flame simulations offer challenging conditions for flow-flame-soot interactions, where soot is formed, matured, advected, and oxidized in an intermittent way comparable to the soot evolution in turbulent flames. Moreover, as a step towards application to more realistic, multi-dimensional flow configurations, the assessment of the FGM-CDSM is extended to a two-dimensional laminar coflow diffusion flame. Finally, the computational performance of the proposed FGM-CDSM method is evaluated.

2. FGM-CDSM methodology

The FGM method [20,21] is an efficient chemical reduction technique based on the concept that multi-dimensional flames can be considered as an ensemble of 1-D flamelets [22]. In FGM, a manifold representing the thermophysical and chemical space, parameterized by relevant control variables, is constructed from the flamelet solutions. The manifold is subsequently coupled to a flow solver through the transport of controlling variables that describe the manifold structure in composition space, so a cost-efficient method for solving multi-dimensional reactive flow simulations is defined [21].

The FGM-CDSM strategy essentially uses the soot chemistry information obtained by the flamelets and recovers the original PSD during run-time (or post-CFD) by transporting only a few clustered sections. The non-linear dependence of different soot subprocesses with sectional soot mass fractions is not explicitly solved in CFD calculation but included in flamelet computations. Therefore, the description of soot formation and PSD in multidimensional flames is assumed to follow their steady flamelet behavior, as the inter-sectional dependence of soot formation rates is implicitly accounted for in the flamelet stage. On the premise of this approach, modeling soot formation with FGM-CDSM involves four key steps:

1. Computation of flamelets including detailed soot kinetics
2. Creation of manifold

3. Coupling the manifold to a CFD solver
4. Re-construction of the soot PSDF

These steps are explained in the following sections.

2.1. Computation of flamelets including detailed soot kinetics

In the first step, 1-D laminar flamelets suitable for the combustion system under consideration (premixed/non-premixed) are computed with a detailed gas-phase reaction mechanism and DSM-based soot model. In the DSM soot model, a range of soot particle volume is discretized into a finite number of sections (n_{sec}). Transport equations for soot mass fraction ($Y_{\text{s},i}$) of section i are solved along with equations for the conservation of mass, momentum, and energy. Under a steady flamelet formulation, the 1-D description of the conservation equations for $Y_{\text{s},i}$ read:

$$\frac{\partial(\rho u Y_{\text{s},i})}{\partial x} = \frac{\partial}{\partial x}\left(-\rho V_{\text{T}} Y_{\text{s},i} + \rho D_{\text{s}} \frac{\partial Y_{\text{s},i}}{\partial x}\right) + \dot{\omega}_{\text{s},i} - \rho G Y_{\text{s},i} \quad ; \quad \forall\ i \in [1, n_{\text{sec}}] \tag{1}$$

where $\rho, u, V_{\text{T}}, D_{\text{s}}, \dot{\omega}_{\text{s},i}$ denote gas density, velocity, thermophoretic velocity, soot diffusion coefficient (assumed to be constant for all particle sizes), and sectional source term, respectively. The strain field G accounts for the flow component in the direction tangential to the flame surface. The sectional soot source terms are computed by considering the contributions of soot nucleation, PAH condensation, surface growth, oxidation, and coagulation sub-processes [4]. Soot nucleation is modeled from PAH dimerization (pyrene here). PAH condensation is assumed to occur through the Brownian collisions between soot particles and PAH. The surface growth and oxidation of soot particles are described through the H-Abstraction C_2H_2-Addition (HACA) mechanism [23,24]. The coagulation model of Kumar and Ramkrishna [25] is utilized to describe the soot particle dynamics. A detailed description of the soot model and its validation can be found in recent works [4,26].

2.2. Creation of manifold

In the second step, a manifold is constructed from the computed flamelets to describe the thermochemical evolution of the flame and the soot chemistry. Important thermo-chemical parameters $\psi(\phi_j)$ of the system are then mapped onto the control variables (ϕ_j) and stored in the flamelet manifold, following the procedure described in van Oijen et al. [21]. As mentioned earlier, the FGM-CDSM method relies on the tabulation of soot source terms. Therefore, the soot source terms for the clusters are stored in the database as functions of the manifold control variables (typically mixture fraction and progress variable) in addition to the transport properties, and relevant gas-phase species.

In the FGM-CDSM method, the number of sections n_{sec} utilized during the computation of the flamelets are combined into a set of clusters n_{clust} for the transport of soot in the CFD simulation. The soot mass fraction ($Y_{\text{s},c}^{\text{clust}}$) in cluster c is, thus, the sum of $Y_{\text{s},i}$ from the original sections that are grouped together in c:

$$Y_{\text{s},c}^{\text{clust}} = \sum_{i=i_c^{\min}}^{i_c^{\max}} Y_{\text{s},i} \tag{2}$$

where $i_c^{\min}$ and $i_c^{\max}$ are, respectively, the lower and upper limit of the sections i that are clustered. The clustering of sections relies on the assumption that soot particles within the cluster preserve the intra-sectional distribution of soot mass exhibited by the associated original sections. In other words, this assumption means that the evolution of the full soot PSD partially depends on the CFD (through the transport of soot clusters) and the FGM tabulation (via re-construction).

For a preliminary assessment of the FGM-CDSM, a uniform clustering of sections is employed. The schematic presentation of the uniform clustering approach is depicted in Fig. 1. Accordingly, the sectional limits of cluster c are given by:

$$i_c^{\max} = c(n_{\text{sec}}/n_{\text{clust}}) \quad ; \quad n_{\text{sec}}/n_{\text{clust}} \in \mathbb{N} \tag{3a}$$

$$i_c^{\min} = i_{c-1}^{\max} + 1. \qquad \forall\ c \in [1, n_{\text{clust}}] \tag{3b}$$

To parameterize the reduction in sectional dimensions, a clustering factor $\mathcal{R}$ is introduced as:

$$\mathcal{R} = 1 - (n_{\text{clust}}/n_{\text{sec}}) \quad ; \qquad \mathcal{R} \in [0, 1) \tag{4}$$

which is zero when no clustering is applied and approaches unity when all sections are grouped into a single cluster.

Owing to the long characteristic time scales of soot formation compared to the fuel-oxidation chemistry, the steady-state assumption of soot chemistry can lead to its inaccurate prediction by flamelet-based approaches [27], yielding non-physical, surplus consumption of soot. A linear relaxation is applied to the soot consumption rate term to prevent this. Consequently, the chemical source terms for the cluster are recast as:

$$\dot{\omega}_{\text{s},c}^{\text{clust}} = \left[\dot{\omega}_{\text{s},c}^{\text{clust},+}\right]^{\text{tab}} + Y_{\text{s},c}^{\text{clust}} \cdot \left[\frac{\dot{\omega}_{\text{s},c}^{\text{clust},-}}{Y_{\text{s},c}^{\text{clust}}}\right]^{\text{tab}} \tag{5}$$

where the superscript tab refers to tabulated quantities. The terms, $\dot{\omega}_{\text{s},c}^{\text{clust},+}$ and $\dot{\omega}_{\text{s},c}^{\text{clust},-}$ for the cluster are given by:

$$\dot{\omega}_{\text{s},c}^{\text{clust},+} = \sum_{i=i_c^{\min}}^{i_c^{\max}} \max(\dot{\omega}_{\text{s},i}, 0), \tag{6a}$$

$$\dot{\omega}_{\text{s},c}^{\text{clust},-} = \sum_{i=i_c^{\min}}^{i_c^{\max}} \min(\dot{\omega}_{\text{s},i}, 0). \tag{6b}$$

The choice of linear relaxation stems from the fact that in the retained soot model, rates of different soot subprocesses scale distinctly with soot mass fraction, in a linear (condensation, surface growth, oxidation) and a quadratic manner (coagulation). Since soot oxidization is the dominant subprocess in overall soot mass consumption, a linear relaxation model appears to be a reasonable approximation for soot consumption rates. Note that no relaxation model is applied to soot production terms, thus soot formation rates are approximated to be correlated with control variables only, following their flamelet values. In this approximation, the non-linear dependence of the soot source term on the soot variable is fully accounted for in the flamelet calculations, instead of CFD. This approximation is carefully verified here for its applicability/deficiencies in several conditions, which will be discussed later. Furthermore, as a modeling choice, in Eq. (5), contributions of the net soot source term are preferred over individual subprocesses. However, it is also possible to isolate the rates of various subprocesses in the tabulation. It is worth highlighting that for slowly evolving species such as PAH, the limitations of the linear relaxation model in flamelet methods have been identified [28]. Nevertheless, in the context of the tabulated source term approach applied here, the relaxation models developed for PAH transport may not strictly hold for the soot mass fractions as PAHs are not used explicitly in the soot source term computation.

2.3. Coupling the manifold to a CFD solver

During the CFD calculation, transport equations are solved for momentum, continuity, enthalpy, manifold control variables (ϕ_j), and the mass fraction of soot in n_{clust} clusters. The transport equations for control variables ϕ_j can be expressed in general form as:

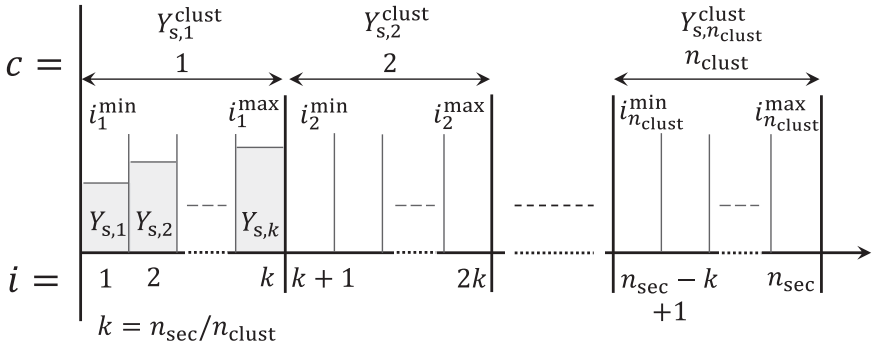

Fig. 1. Schematic diagram of the uniform clustering in the FGM-CDSM method.

$$\frac{\partial\left(\rho\phi_j\right)}{\partial t} + \nabla\cdot\left(\rho\boldsymbol{u}\phi_j\right) - \nabla\cdot\left(\frac{\lambda}{c_p}\nabla\phi_j\right) = \nabla\cdot\left(\mathcal{D}_{\phi_j}\nabla\phi_j\right) + \dot{\omega}_{\phi_j} \tag{7}$$

where λ, c_p, $\dot{\omega}_{\phi_j}$, $\mathcal{D}_{\phi_j}$, respectively denote thermal conductivity, specific heat capacity, source term, and preferential diffusion coefficient. The transport equation for the clustered soot mass fraction derived from Eqs. (1) and (2), can be expressed in a general form as:

$$\frac{\partial\left(\rho Y_{s,c}^{clust}\right)}{\partial t} + \nabla\cdot\left(\rho[\boldsymbol{u}+\boldsymbol{V_T}]Y_{s,c}^{clust}\right) = \nabla\cdot\left(\rho D_s\nabla Y_{s,c}^{clust}\right) + \dot{\omega}_{s,c}^{clust}. \quad \forall\ c\in[1,n_{clust}] \tag{8}$$

The source term $\dot{\omega}_{s,c}^{clust}$ is calculated following Eq. (5). The thermo-chemical variables (ψ) required for the solution of Eqs. (7) and (8) are retrieved from the flamelet manifold as a function of the control variables.

2.4. Re-construction of the soot PSDF

After calculation of the chemical states in the CFD simulation, the distribution of soot mass fraction within the n_{sec} sections is re-constructed from the tabulated $Y_{s,i}$ and the computed $Y_{s,c}^{clust}$, via the expression:

$$Y_{s,i}^{re} = \left[\mathcal{F}_i(\phi_j)\right]^{tab}\cdot Y_{s,c}^{clust} \tag{9}$$

with $\mathcal{F}_i$ the mass fraction of section i in cluster c given by:

$$\mathcal{F}_i = \frac{Y_{s,i}}{\sum_{i=i_c^{min}}^{i_c^{max}} Y_{s,i}}. \tag{10}$$

This fraction is assumed to be a function of the control variables (ϕ_j) only and is provided in the database as a lookup variable for the re-construction of the sectional soot mass fractions $Y_{s,i}^{re}$. Subsequently, relevant soot quantities such as number density, mean particle diameter, and PSDF can be derived from the re-constructed sectional soot mass fractions using the appropriate relations (Ref. [4]). Note that the re-construction of soot PSDF can be achieved in a post-processing step or in run-time. A schematic of the aforementioned steps is presented in Fig. 2.

3. Assessment of FGM-CDSM for 1-D laminar flames

The performance of the FGM-CDSM approach is first evaluated in simulations of 1-D laminar counterflow diffusion flames under steady and unsteady conditions.

3.1. Flamelet tabulation approach

In all the 1-D laminar flames investigated in the present study, the same strategy is employed for manifold construction. A series of strained steady flamelets including soot chemistry are computed with $n_{sec} = 60$ using the code CHEM1D [29]. This value for n_{sec} presents a good compromise between computational cost and model accuracy based on preliminary sensitivity studies [30]. To generate a steady branch of the manifold, the applied stain rate is varied from lower values (close to chemical equilibrium) until the extinction limit for the corresponding flame. Subsequently, the composition space between the extinction limit and mixing solution is covered by simulating unsteady extinguishing flamelet, which is also embedded in the manifold as a continuation of the steady branch. The detailed kinetic scheme KM2 of Wang et al. [31], involving 202 species and 1351 reactions, is used for the gas phase chemistry during the computation of flamelets. The diffusion transport of species is modeled using a mixture-averaged approximation [32]. Here we consider non-premixed flames for the assessment of the FGM-CDSM strategy. Therefore, for FGM simulations, the mixture fraction (Z) and reaction progress variable ($\mathcal{Y}$) are selected as suitable control variables. The Z definition follows the work of Bilger [33], while $\mathcal{Y}$ is represented by a linear combination of suitable species as:

$$\mathcal{Y} = \sum_j \alpha_j Y_j \tag{11}$$

where α_j and Y_j are, respectively, weight factor,and mass fraction of the species j. Here, $\mathcal{Y}$ is defined based on H_2O, CO_2, CO, O_2, H_2, and A4 species mass fractions with their corresponding weight factors $\alpha_{H_2O} = 0.0555$, $\alpha_{CO_2} = 0.0228$, $\alpha_{H_2} = 0.173$, $\alpha_{CO} = 0.0357$, $\alpha_{A4} = 0.0988$, $\alpha_{O_2} = -3.13\times10^{-4}$. The progress variable definition is determined using a guess-and-check approach based on previous experience, and this selection should be taken with care. This definition has been applied in previous work [16] and shown to preserve the unique mapping of $\mathcal{Y}$ in composition space. The inclusion of slow chemical species such as A4 in $\mathcal{Y}$ is shown to improve the mapping of its chemical source term evolution in FGM [16], therefore, the aforementioned $\mathcal{Y}$ definition is retained here. Nevertheless, it is also noticed that in the case of the tabulation of soot source terms (FGM-CDSM), the accuracy of soot prediction is almost insensitive to the inclusion of A4 species in $\mathcal{Y}$. The manifolds are discretized with 400×400 equally-spaced grid points in the Z and $\mathcal{Y}$ directions, respectively.

3.2. Steady non-premixed counterflow flames

The FGM-CDSM approach is applied to 1-D steady counterflow diffusion flames from literature [34–36]. This is generic but a crucial step in the context of identifying the lookup-related errors,

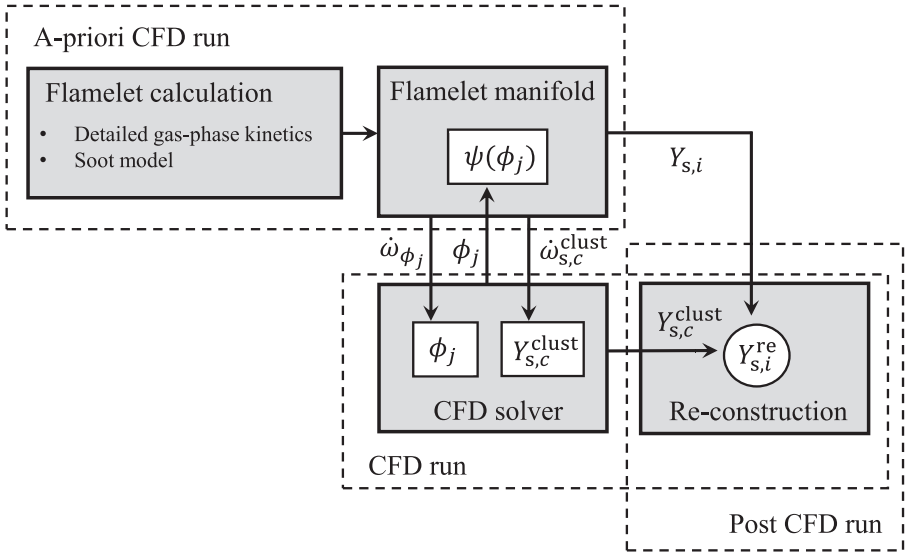

Fig. 2. An overview of the key steps in the FGM-CDSM method.

Table 1
Investigated counterflow flames.

Flame	Fuel $X_{C_2H_4}$ / X_{N_2}	Oxidizer X_{O_2} / X_{N_2}	Reference
CDF-1	1.0 / 0.0	0.25 / 0.75	Wang et al. [34]
CDF-2	0.8 / 0.2	0.25 / 0.75	Wang and Chung [35]
CDF-3	1.0 / 0.0	0.30 / 0.70	Xu et al. [36]

and examining the suitability of control variable definitions. The details of the target flames considered for the assessment are summarized in Table 1. Owing to the different compositions of reactants, individual flamelet manifolds are created for the different flames in Table 1.

Comparisons in soot volume fraction (f_v) between the experimental measurements, detailed chemistry (DC), and FGM-CDSM are presented in Fig. 3 for the target flames. The numerical prediction of f_v for both DC and FGM agrees well with the experimental measurements on the different cases. The f_v profiles computed with FGM-CDSM favorably reproduce their DC counterparts, and the change in clustering factor $\mathcal{R}$ shows only a marginal impact on the accuracy of FGM-CDSM. To illustrate the merits of the FGM-CDSM in detail, key global soot quantities computed with DC and FGM are compared in Fig. 4 as a function of Z for the CDF-1 flame. The profiles of soot number density (N) and average particle diameter (D_{avg}) reconstructed through FGM-CDSM exhibit a good agreement with DC results. The departure from DC solutions for

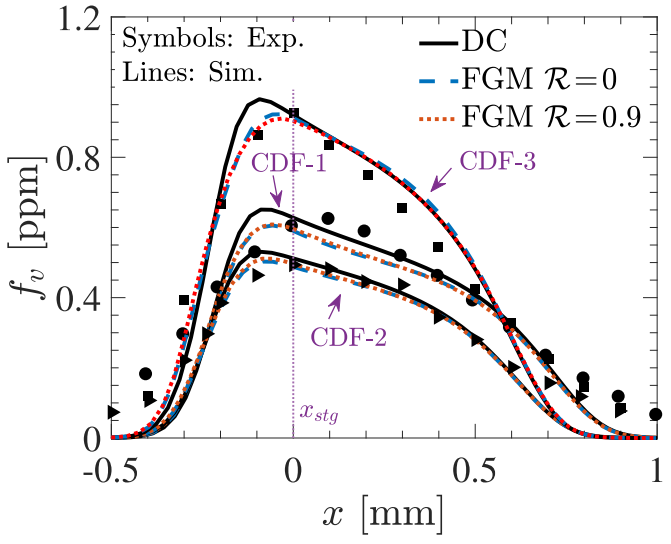

Fig. 3. Comparison of numerical results of f_v with DC and FGM-CDSM against experiments [34–36].

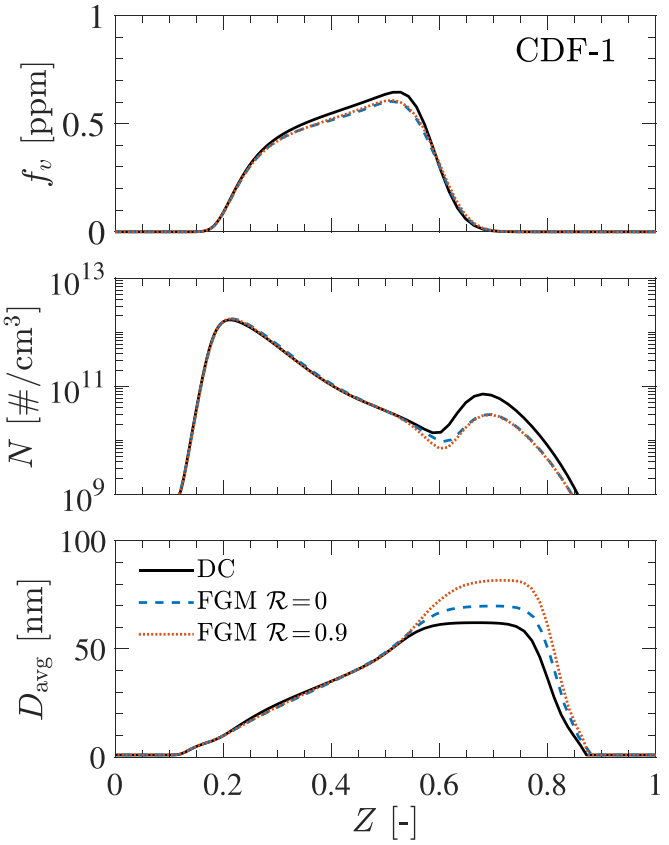

Fig. 4. Comparison of global soot quantities f_v, N, and D_{avg} predicted by DC and FGM-CDSM simulations.

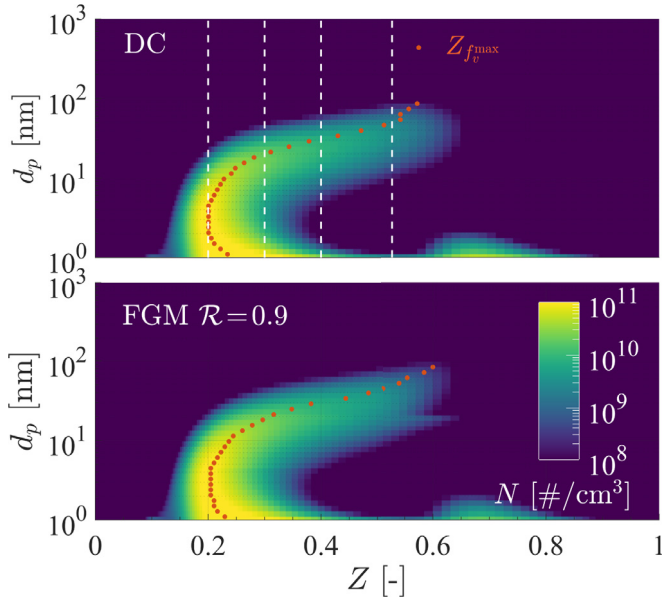

(a)

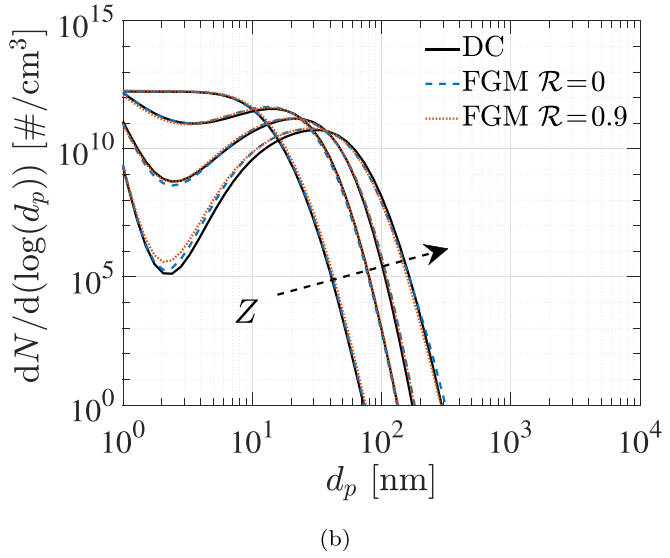

(b)

Fig. 5. Comparison of N distributions in $Z-d_p$ space (a), and profiles of soot PSDFs at $Z=0.2$, 0.3, 0.4, $Z_{f_v^{max}}$ positions (b) for DC and FGM-CDSM. The position of maximum f_v in $Z-d_p$ space is marked by orange dots in subplot (a) and dashed white lines correspond to Z locations of PSDFs.

$\mathcal{R}=0$ (no clustering) essentially highlights the role of FGM chemistry. Such discrepancies mainly arise from the progress variable definition and interpolation-related errors introduced during the retrieval of manifold quantities, especially the soot source terms. Note that, the departure from DC results for $Z>0.6$ are the result of a small peak in the PAH predicted by the employed chemical kinetic scheme [37].

As part of the assessment, it is imperative to verify the assumption of PSD preservation within the soot clusters. To address this, the $Z-d_p$ distribution of re-constructed soot number density for $\mathcal{R}=0.9$ is compared against the DC results in Fig. 5(a). As can be noticed, the FGM-CDSM approach reproduces well the N distribution of the DC simulations. In addition, the locations of f_v^{max} in $Z-d_p$ space are also well captured by FGM-CDSM. Finally, the evolution of soot PSDF reconstructed from FGM-CDSM is compared against DC solutions for different Z positions in Fig. 5(b). The evolution of soot PSDF predicted by the FGM-CDSM approach is in

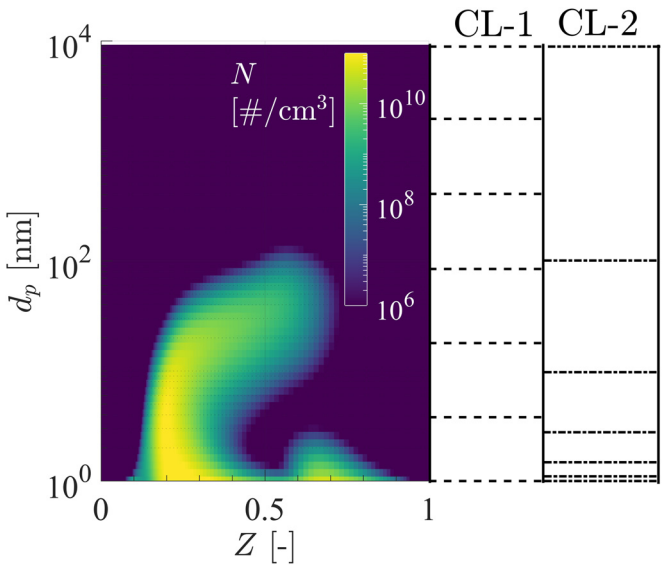

Fig. 6. Distributions of soot number density in $Z-d_p$ space (left panel), and the size limits of sections considered in uniform (CL–1) and non-uniform (CL–2) clustering (right panel).

good agreement with the DC and no-clustering solutions. Moreover, the transition from unimodal to the bimodal shape of PSDF with increasing Z is well reproduced by the re-constructed soot sections. It is also clear from the numerical results that the accuracy of soot prediction is only slightly impacted by the application of clustering. Overall, the analysis of predicted soot quantities and size distributions for steady 1-D flames exemplify the favorable ability of the clustering approach in reproducing the evolution of not only the global soot quantities but also the PSDF of the original sections.

It is important to note that the uniform clustering considered in the current work is purely an operational choice. Therefore, it is also interesting to investigate the impact of clustering distribution on the accuracy of FGM-CDSM. To address this, a non-uniform clustering of sections is formulated with identical $\mathcal{R}=0.9$ (6 clusters). The distribution of particle sizes in uniform (referred to as CL-1 here) and non-uniform (referred to as CL-2) clusters is shown in Fig. 6. As can be observed, the cluster size is smaller near the small particle sizes for CL-2 (where soot number density is typically higher) and progresses approximately with a geometrical fraction.

The profiles of f_v are compared in Fig. 7(a) for different clustering distributions at several strain rates (a). The qualitative prediction of f_v response to strain rate variation with FGM-CDSM is encouraging. However, discrepancies between FGM and DC solutions can be noticed for the lowest strain rate. Furthermore, slight differences in the f_v profiles are apparent for different clustering distributions. For the CL-2 distribution, the f_v profiles are somewhat underpredicted compared to CL-1 and DC. The sensitivity of FGM-CDSM to clustering distribution may be attributed to a coarser representation of sections, which predominantly contributes to the overall soot volume fraction. For instance, in the case of CL-2, the sections corresponding to $d_p>10$ nm are represented by 2 clusters, while for CL-1, the same range of particle size encompasses approximately 4 clusters. The difference in cluster sizes may lead to discrepancies in the retrieval of the net soot source term of the cluster and, eventually, the soot volume fraction. At lower strain rates, the soot source terms are primarily concentrated within larger sections owing to higher residence time and facilitating sustained growth of soot particles. Hence, higher sensitivity of FGM-CDSM to clustering distribution is found at lower strain rates.

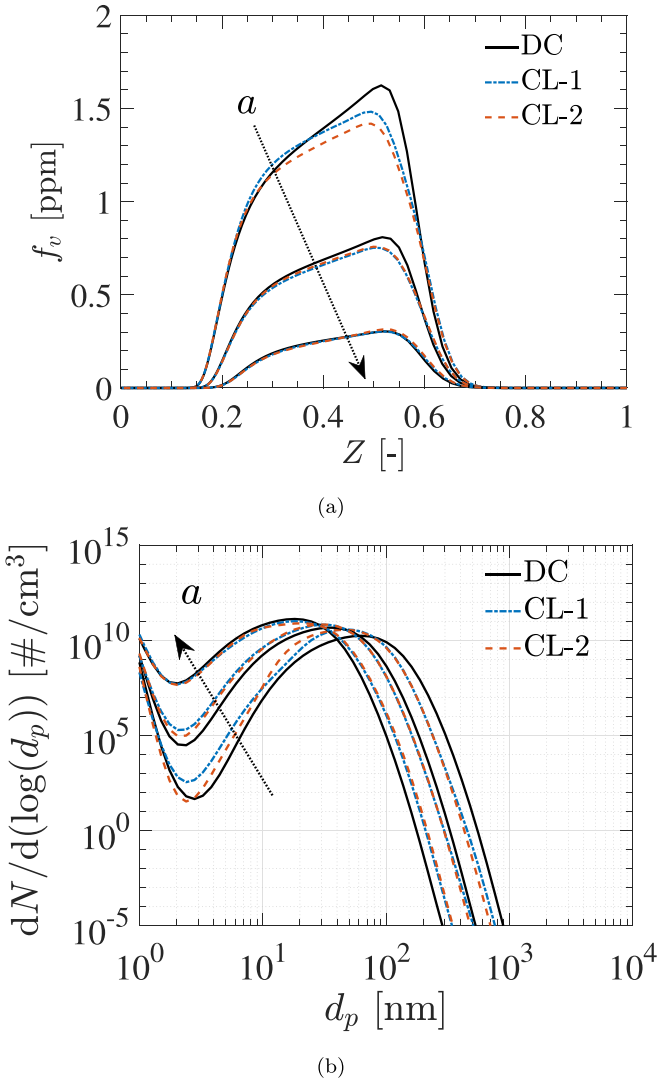

Fig. 7. Profiles of soot volume fraction (a), and particle size distribution function (PSDF) at peak f_v position (b) for CL-1 and CL-2 clustering at $a = 50, 100, 200$ s^{-1}. Arrow points in the increasing direction of the strain rate.

In addition to the soot volume fraction, it is also essential to examine the impact of clustering distribution on the re-constructed soot PSDF. Hence, the profiles of soot PSDF at maximum f_v position are compared for the two clustering distribution types in Fig. 7(b). It can be observed that the clustering distribution influences the prediction of soot PSDF. Under the CL-2 distribution, the PSDFs show close agreement with DC profiles near the trough of the PSDF for a range of strain rates as compared to the CL-1 distribution. As mentioned earlier, the finer distribution of clusters in the lower particle sizes for CL-2 tends to improve the accuracy of PSDF prediction within the power-law mode of the PSDF. The analysis suggests that the accuracy of FGM-CDSM is impacted by the clustering distribution, especially at lower strain rates. Although the uniform clustering appears to perform fairly well for different $\mathcal{R}$, a more sophisticated non-uniform clustering facilitating fine cluster sizes within smaller sooting sections might improve the accuracy of the FGM-CDSM. In the context of practical applications, the qualitative agreement between FGM and DC for different clustering distributions seems reasonable. Hence, a dedicated study on the optimization of clustering distribution is not considered in the present work.

3.3. Unsteady non-premixed counterflow flames

Tabulated chemistry methods are commonly applied to simulations of turbulent flames, which are inherently unsteady and often manifest strong variations of local strain rates. Therefore, it is important to investigate the predictive capabilities of FGM-CDSM in capturing the dynamic evolution of soot in such transient conditions. Two unsteady conditions are considered for this assessment. These cases are described in the following subsections.

3.3.1. Flames with oscillating strain rates

To represent an important aspect of unsteady flow evolution, simulations are carried out for non-premixed counterflow flames subjected to oscillations of strain rate. Such an unsteady configuration essentially mimics the fluctuating flow field through imposed strain rate oscillations. The sufficiently fast fluctuations of the flow field lead to an almost instantaneous variation of local stretch rate in a counterflow burner, and gas-phase chemistry as well as soot chemistry tend to adjust to the transient conditions. Hence, the counterflow flame configuration with imposed harmonic oscillations in the strain rate has been conveniently used to investigate the effects of hydrodynamic unsteadiness on the soot and PAH formation in previous works [38–40]. Here, this configuration is retained to examine the capabilities of FGM-CDSM in predicting the dynamic response of soot to flow unsteadiness when a flame that is in a steady-state is subjected to strain rate fluctuations.

The laminar counterflow flames experimentally investigated by Li et al. [41] are considered for this assessment. In these flames, the fuel stream is pure ethylene, and the oxidizer is composed of 25–75% O_2-N_2 on a volume basis. The strain rate unsteadiness is introduced by imposing sinusoidal fluctuations to the fuel and oxidizer velocities at frequency f with an amplitude A_u around a mean global strain rate. The global strain rate K_g definition is based on oxidizer stream velocity u_o and nozzle separation distance L as Cuoci et al. [38]:

$$K_g = \frac{4u_o}{L}. \tag{12}$$

The velocity fluctuations imposed to the oxidizer stream have the following form:

$$u_o(t) = u_o^{st}[1 + A_u \cdot \sin(2\pi f t)], \tag{13}$$

where u_o^{st} is the steady-state value of the inlet velocity of the oxidizer stream. The profile for fuel stream fluctuations is obtained by fitting their measured values. Initially, the flame is in a steady state at $K_g = 144$ s^{-1}, and the corresponding solution presents the initial condition for the application of the sinusoidal oscillations. The imposed variations of nozzle exit velocities with time for the fuel and oxidizer with $f = 60$ Hz, and $A_u = 50\%$ are shown in Fig. 8 along with experimental measurements from Li et al. [41].

In Fig. 9, the dynamic response of soot volume fraction peak values (f_v^{max}) is presented against the dimensionless time ($\tau = ft$) for DC and FGM simulations. In addition, measured values of unsteady f_v^{max} and K_g are plotted for comparison. Consistent with previous studies [38], for an increase in the imposed frequency, the amplitude of induced oscillations of soot volume fraction tends to decrease, while the phase-lag between imposed oscillations and soot response becomes larger. It can be observed that DC results show very good agreement with measurements for the transient soot response. The maximum and minimum values of the induced soot oscillations quantitatively match well with their experimental values, although a slight phase-lag can be observed for the simulation. For the first time, the transient response of soot predicted by DSM is compared against experiments, and the results suggest that the retained soot model captures the dynamic response of soot with good qualitative and quantitative agreement. In addition to

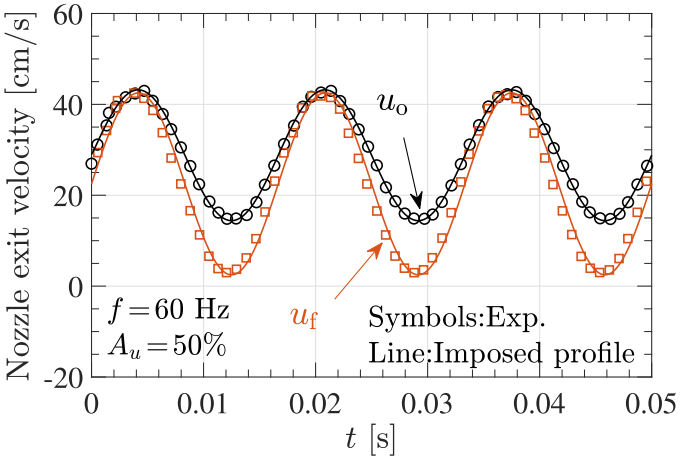

Fig. 8. Comparison of measured [41] and numerically imposed evolution of oxidizer (u_o) and fuel (u_f) nozzle velocity as a function of time (t) with $f = 60$ Hz, and $A_u = 50\%$.

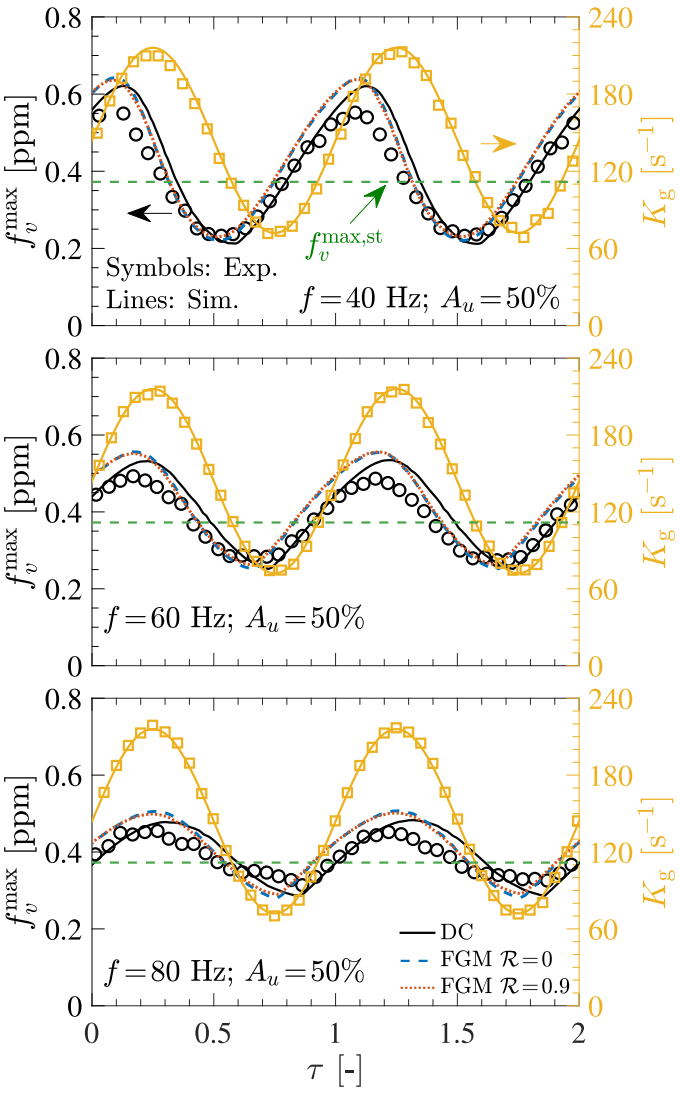

Fig. 9. Measured (symbols) [41] and computed (lines) temporal evolution of K_g and maximum soot volume fraction (f_v^{max}) as a function of dimensionless time $\tau = ft$ in unsteady counterflow flames.

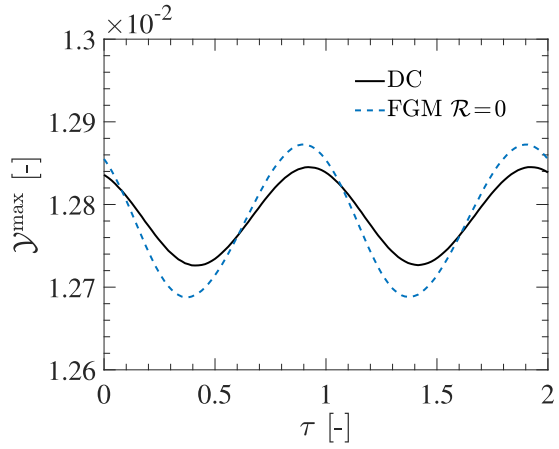

Fig. 10. Comparison between DC and FGM solutions for transient evolution of peak $\mathcal{Y}$ for $f = 60$ Hz case.

DC, the dynamic response of soot is also reproduced reasonably well by the FGM-CDSM method. The amplitude and the peak values of the induced oscillations agree well with the DC and experimental results. It is also evident that the FGM profiles for soot response with clustering ($\mathcal{R} = 0.9$) are almost identical to the one achieved without the inclusion of clustering, see Fig. 9. Nevertheless, the transient variation of f_v^{max} for FGM chemistry is found to be in better agreement with experiments, while DC tends to overpredict the phase-lag. In FGM simulations, variation in local flame structure with unsteady strain rate is essentially represented through the response of control variables to the imposed fluctuations. Since control variables are used to parameterize various thermochemical parameters from the manifold that is generated from steady flamelets at different strain rates, (and extinguishing flamelets) the unsteady phase lag, and soot attenuation is a consequence of the flamelet behavior of soot source terms (through the progress variable) along with transport. To elucidate this argument, the transient evolution of the progress variable for the DC and FGM is shown in Fig. 10. The phase-lagged response of the progress variable can be noticed in DC results compared to FGM, which essentially translates into phase-lag in the unsteady evolution of f_v^{max}. In the current FGM-CDSM framework, manifolds are constructed through steady and extinguishing flamelets. An extension of the manifold generated from fluctuating flamelets with additional parametrization, as proposed in the work of Delhaye et al. [42], or an unsteady flamelet formulation, introduced by Pitsch and Imhe [43] can also be considered to improve the accuracy of soot prediction in the unsteady conditions.

To demonstrate the ability of FGM-CDSM in capturing unsteady soot evolution, the instantaneous profiles of re-constructed PSDF are compared against DC solutions in Fig. 11. The PSDFs are taken at the temporal positions denoting the maximum and minimum of the induced soot response and at the spatial location of the maximum soot volume fraction for different imposed frequencies. In a counterflow configuration, a decrease in strain rate tends to increase the residence time of soot particles, which enhances their growth through surface reactions and coagulation. Consequently, the log-normal mode of PSDF shifts towards larger particle diameters while the trough of the PSDF moves toward lower particle number densities. The opposite occurs for the increase in the strain rate. It is evident from Fig. 11 that the FGM-CDSM tends to qualitatively reproduce the PSDF shape from DC. The application of clustering reproduces well the unsteady PSDF evolution when compared to the case without clustering, which displays the potential of FGM-CDSM to capture the dynamic evolution of the soot PSDF.

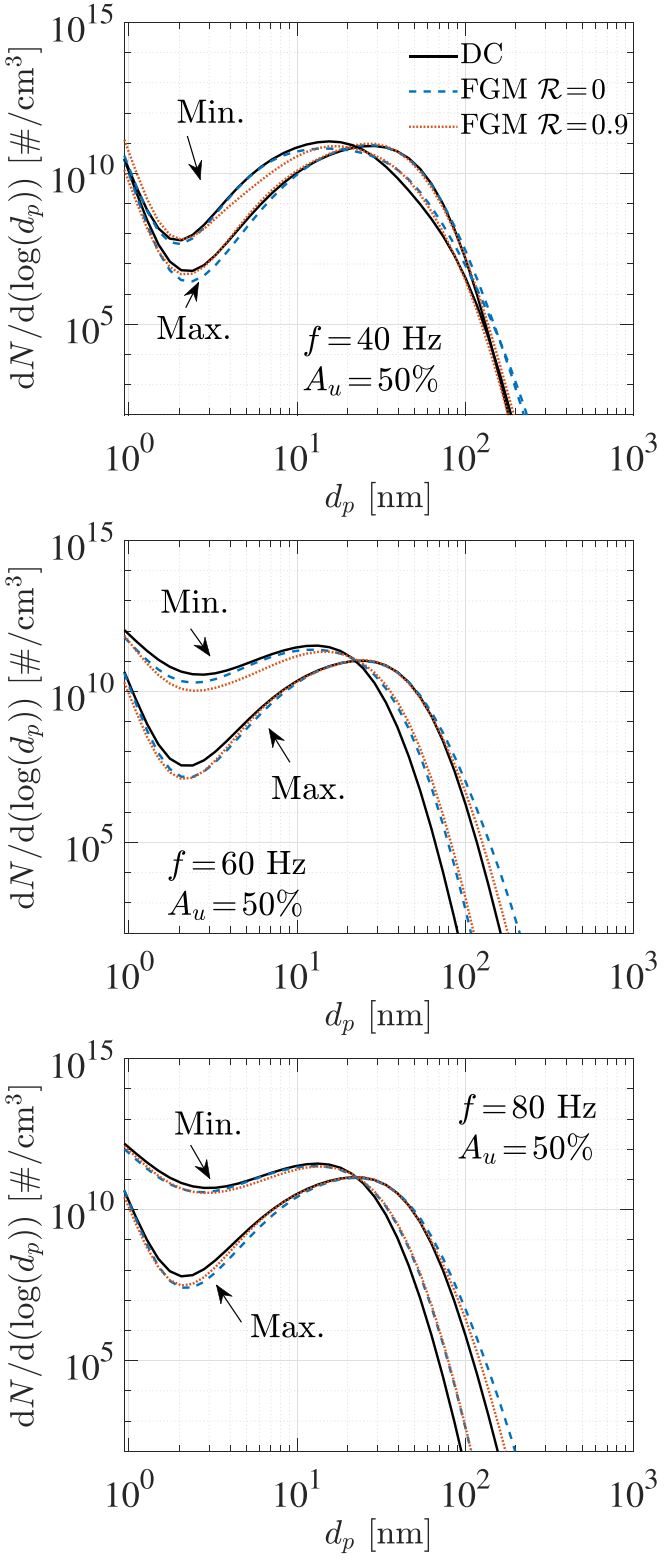

Fig. 11. Comparison of soot PSDFs for maximum and minimum values of the induced response taken at $f_v^{\max}$ locations for DC and FGM chemistry under different frequencies.

Considering the modest range of frequency (30-80 Hz) employed in the experiments [41], the attenuation observed in soot response is relatively small. Hence computations are performed for higher frequencies of imposed strain rate oscillations. The comparison of peak soot volume fraction response between FGM-CDSM ($\mathcal{R}=0$) and DC for several frequencies is presented in Fig. 12(a).

The phase-lag in the response of soot to the imposed fluctuations is prominent at higher frequencies, accompanied by a drastic reduction in the amplitude of the soot oscillations. Such strong attenuation of soot oscillations at substantially higher frequencies is captured well by the FGM-CDSM approach. As can be observed in Fig. 12(b), the amplitude of induced oscillations in peak soot volume fractions ($\Delta f_v^{\max}$) obtained with FGM-CDSM agree well with their DC counterparts, which demonstrate good capabilities of FGM-CDSM in capturing soot formation under unsteady conditions. It is worth highlighting that at very high frequencies (e.g., 500 Hz) the oscillation times are very small. These flow oscillations introduce rapid variations in radical formation due to strain effects but occur at smaller time scales than those of the soot chemistry. As the frequency of the perturbations increases, the amplitude of the response in soot formation reduces to zero. While this tendency is well predicted, certain discrepancies appear concerning the dynamic response to flow oscillations. A phase-lag between DC and FGM solutions can be distinguished in Fig. 12(b). This response is associated with the strategy used for flamelet tabulation and manifold generation.

3.3.2. Unsteady soot evolution from gas phase

In the FGM-CDSM approach, the soot source terms are calculated and stored for soot mass fractions (and other variables) in steady state. Therefore, the chemical trajectories concerning the formation of soot from the gas phase to the steady state are not explicitly retained in the FGM manifold. Hence, it is also interesting to investigate the capabilities of FGM-CDSM in predicting the unsteady formation of soot from the pure gas phase. The time-dependent evolution of soot volume fraction from an initial condition pure gas-phase initial solution (i.e., steady solution with $Y_{s,i}=0$) for $\mathcal{R}=0$ and $\mathcal{R}=0.9$ are compared against the DC counterparts in Fig. 13(a) for the CDF-1 flame investigated earlier in Section 3.1. It can be observed that the soot evolution at the early-stage is not very well captured by the tabulation of the soot source terms ($\mathcal{R}=0$). However, the influence of clustering ($\mathcal{R}=0.9$) on f_v profiles at different time instances is found to be negligible.

At smaller time intervals (0.005 to 0.1 ms), the comparison between FGM-CDSM and DC profiles in Fig. 13(b) shows a significant overprediction (up to a factor of 4) of soot volume fraction by FGM-CDSM. However, the clustering of sections accurately reproduces the soot volume fraction profiles of their no-clustering counterparts. Apart from the quantitative differences, the soot volume fraction profiles in the region $0.2<Z<0.3$ are found to be more skewed for FGM-CDSM than DC. This response can be attributed to the fact that the soot source term is obtained from steady flamelets, resulting in an overprediction of growth (by condensation and surface reactions mainly) within $0.2<Z<0.3$. In contrast, for DC, soot inception is more prevalent in earlier times, resulting in more distributed f_v profiles in the mixture fraction space, with higher f_v in $0.2<Z<0.3$ compared to FGM-CDSM. This overprediction of soot volume fraction is not unexpected given the lack of information on the chemical trajectories from the gas phase to the steady-state soot evolution in the flamelet database.

The departure from DC results for f_v is primarily related to the tabulation of soot source terms. For flame initially at steady state without soot, the direct look-up of soot production rate in the clustered section ($\dot{\omega}_{s,c}^{\mathrm{clust},+}$) is overestimated, while the linearized consumption rate ($\dot{\omega}_{s,c}^{\mathrm{clust},-}$) is underestimated. Especially, near $Z=0.5$, the f_v values are overpredicted as compared to the DC solutions. This is because, in a counterflow flamelet, the low residence time of soot enhances soot particle size (and volume fraction) as particle approach the stagnation plane (the fuel-rich side for the current case). As a result, the discrepancy in soot profiles is particularly evident near higher mixture fractions. The agreement between DC and FGM-CDSM results for f_v tends to be better as the soot forma-

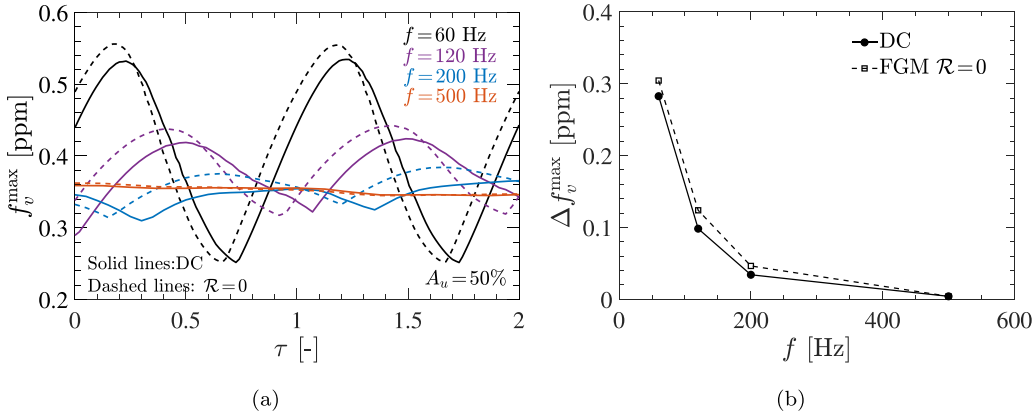

(a) (b)

Fig. 12. Comparison between FGM and DC solutions for transient response of maximum soot volume fraction (f_v^{max}) (a), and amplitude of induced f_v^{max} oscillations (b) in unsteady counterflow flames.

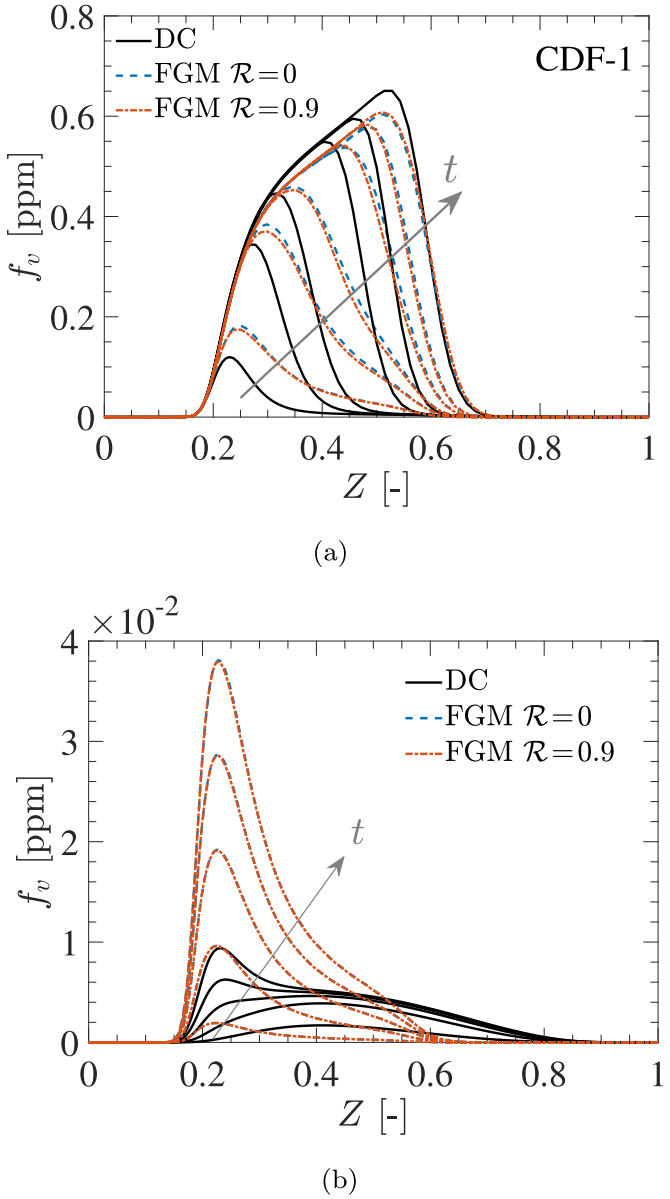

(a) (b)

Fig. 13. Evolution of f_v from steady gas-phase solution for DC and FGM chemistry. Gray arrow indicates time $t = 0.5, 1.5, 2.5, 5, 7.5, \infty$ ms (a), and $t = 0.005, 0.01, 0.05, 0.075, 0.1$ ms (b).

tion progress toward a steady state. Naturally, an extension of FGM to incorporate the chemical trajectories of soot formation (from the gas phase to the steady state) would require computations of complementary unsteady flamelets (at every level of scalar dissipation rate), which would also require an additional controlling variable to entirely encapsulate the reaction progress of soot, leading to a rather complex manifold generation. However, adhering to the scope of the present work, further investigation is neces-

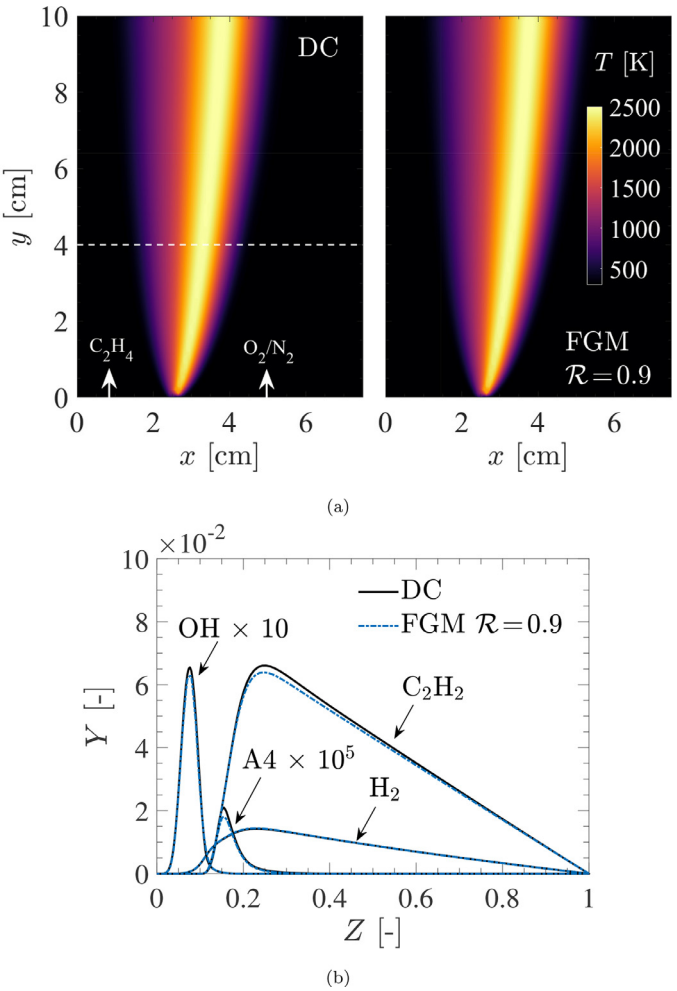

(a) (b)

Fig. 14. Comparison between DC and FGM-CDSM solutions for temperature fields (a), and mass fractions of important gas-phase species at $y = 4$ cm (b).

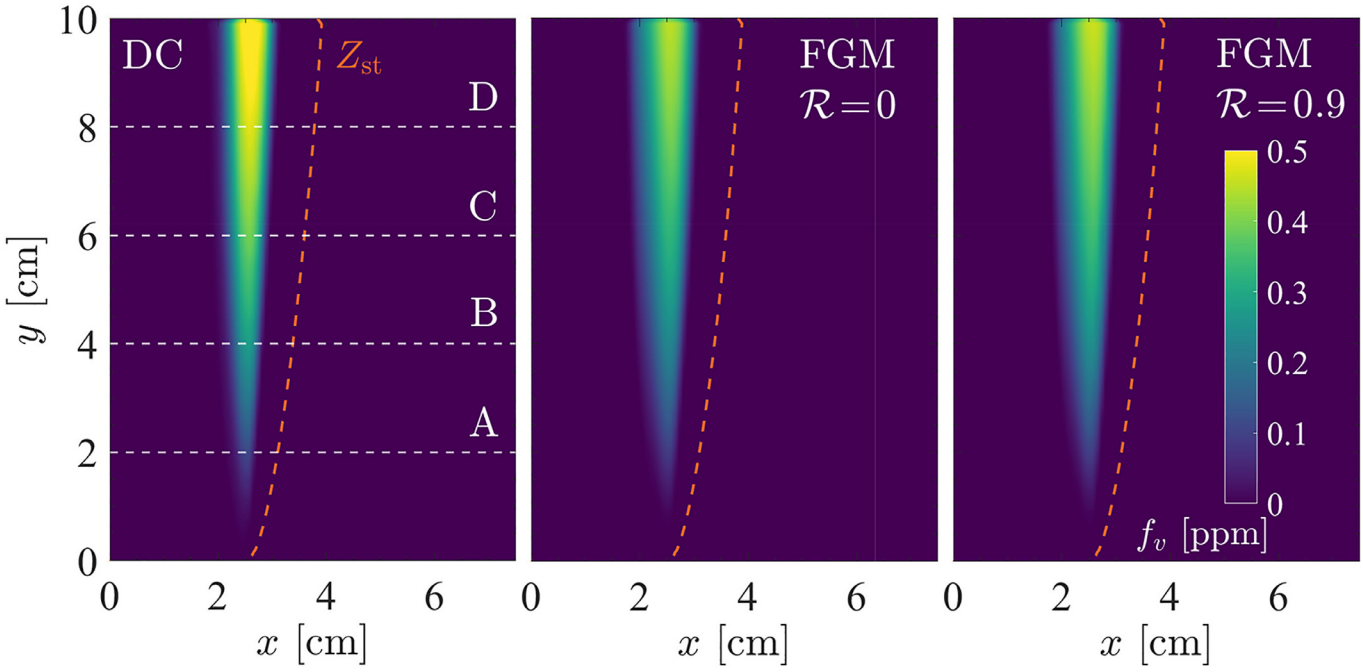

Fig. 15. Comparison between DC and FGM-CDSM solutions for soot volume fraction fields.

sary to fully address this aspect. Note that the simulation starting from no-soot is a special case considered here to demonstrate the limitations of the soot source term tabulation approach. Nevertheless, in simulation applications where the unsteady evolution of soot quantities is not of interest, the no-soot initialization can be replaced with a steady-state soot initial condition.

4. Application of FGM-CDSM for 2-D laminar flames

As a next (intermediate) step towards real burner configurations, a laminar coflow diffusion flame is considered to evaluate the performance of FGM-CDSM. The burner configuration is a 2D planar channel enclosed by adiabatic no-slip side walls and maintained at atmospheric pressure. The geometrical aspects can be seen in Fig. 14(a). The fuel is pure ethylene, and the oxidizer is composed of O_2 and N_2 (25/75 by volume, respectively). The fuel and oxidizer are injected at 15 cm/s and 300 K temperature. The sooting flame simulations with both detailed chemistry and FGM-CDSM are carried out using the multi-physics code Alya [44]. The code Alya has been successfully applied for the investigation of laminar and turbulent flames using tabulated and finite rate chemistry [45–47], and will be used here as a platform for comparing the different approaches for FGM-CDSM. The kinetic mechanism ABF of Appel et al. [24], containing 101 species and 544 elementary reactions, is employed for the detailed chemistry simulation and the computation of the diffusion flamelets. The FGM database is constructed using steady and unsteady quenching counterflow flamelets following the strategy mentioned in Section 3.1. The progress variable definition employed in 1-D flame simulations (presented in Section 3.1) is retained for 2-D simulations. The ABF mechanism is selected solely to reduce the cost of the detailed flame simulations. To further minimize the cost of calculations, $n_{sec} = 40$ sections are considered. The differential diffusion effects are important in sooting flames as demonstrated in earlier works [48,49] and can be included, but for the sake of simplicity in the DC vs FGM comparison, the unity Lewis number assumption is retained here for diffusion transport of gaseous species. The performance of FGM-CDSM has been investigated for non-unity Lewis transport in 1-D cases.

The steady-state contours of temperature for DC and FGM-CDSM are compared in Fig. 14(a). A good agreement between the numerical solutions is shown for the temperature distribution, which probes the ability of the FGM chemistry to capture the flame position. In addition, mass fraction profiles of the key gas-phase species at stream-wise location $y = 4$ cm predicted by detailed kinetics and FGM are presented in Fig. 14(b). The numerical profiles of different species obtained with the FGM chemistry are in good agreement with the detailed simulation. The comparisons of temperature and gas-phase species, confirm that the flame structure is fairly well reproduced by the FGM chemistry in this planar flame configuration.

Subsequent to the verification of the flame structure, the contours of soot volume fraction predicted by DC and FGM-CDSM, are presented in Fig. 15 for $\mathcal{R} = 0$ and $\mathcal{R} = 0.9$. The overall distribution of f_v is well reproduced by FGM-CDSM. Early-stage soot formation near the upstream region is captured well by FGM solutions. However, the FGM-CDSM shows a slight tendency to underpredict peak f_v compared to the DC solution as the flame develops downstream. The profiles of f_v and PSDF at several downstream positions are compared in Fig. 16 for a more quantitative illustration of the accuracy of FGM-CDSM. The qualitative agreement between DC and FGM-CDSM for the prediction of f_v distribution in Z-space is encouraging. Furthermore, the evolution of the soot PSDF along several downstream locations and their bi-modality is re-constructed with reasonable accuracy by FGM-CDSM. However, a quantitative deviation between the DC and FGM-CDSM solutions can still be observed. The f_v profiles predicted by FGM-CDSM tend to exhibit wider distributions in Z-space compared to DC. However, the results clearly show, that the introduction of clustering ($\mathcal{R} = 0.9$) only does not impact the overall accuracy of FGM-CDSM compared to the case transporting all the sections ($\mathcal{R} = 0$). Therefore, the noticed departure from DC solutions suggests the limitation of tabulated source terms to exactly reproduce the chemistry of the soot formation.

It is important to highlight that the FGM database here is generated using steady and unsteady quenching formulations of representative counterflow flamelets. In FGM the soot source terms are calculated and stored for soot mass fractions (and other variables)

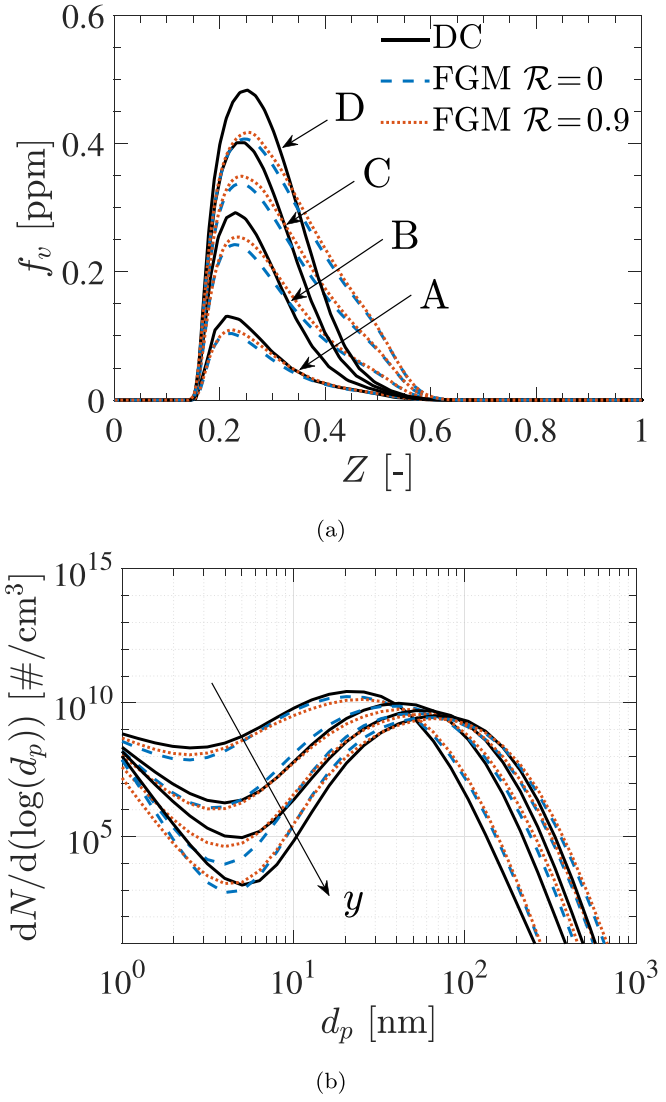

Fig. 16. Comparison between DC and FGM-CDSM solutions for profiles of f_v (a), and PSDF (at $f_v^{\max}$) along $y = 2$, 4, 6, 8 cm (denoted by A, B, C, D, respectively in Fig. 15) downstream positions (b).

in a steady state, while in the coflow case, the soot mass fractions are initially much lower and slowly increase toward steady-state values. Therefore, the chemical trajectories concerning the formation of soot from gas-phase to steady-state are not explicitly retained in the FGM manifold. As already noticed in the results for unsteady soot evolution for 1-D counterflow flame (refer Fig. 13(a)) the early-stage reaction progress of soot is not well captured by the FGM-CDSM method. Especially, near $Z = 0.5$, the f_v values are overpredicted as compared to the DC solutions. A similar trend is also translated near $Z = 0.5$ for the f_v profiles in the 2-D coflow case. Nevertheless, considering the challenges associated with the numerical prediction of soot formation in multi-dimensional flames, the performance of the novel FGM-CDSM approach in capturing soot formation is remarkable.

5. Computational performance

An important aspect of the FGM-CDSM method is its computational efficiency. The efficiency is evaluated here from the computing time required to perform time-dependent simulations of laminar flames for a period of 1 ms. The solutions from FGM-CDSM and DC are compared in Fig. 17. In CHEM1D, a fully implicit 2nd-order time integration scheme with an adaptive time step strategy is considered for simulations of laminar counterflow flames. On the other hand, in Alya, an explicit 3rd-order Runge–Kutta time integration scheme with a constant time step is employed for the assessment of CPU time.

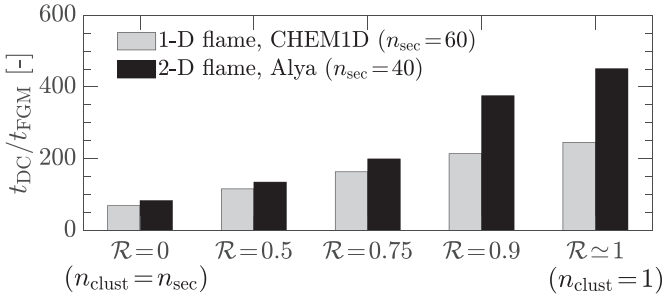

Fig. 17. Computational speed-up with FGM-CSDM for laminar flame simulations in CHEM1D and Alya.

Figure 17 shows that the FGM-CDSM enables a reduction in CPU time by two orders of magnitude compared to detailed chemistry with the same number of sections ($\mathcal{R} = 0$). Clustering of sections leads to further reduction of the computational cost. For instance, in 1-D calculations, a factor 10 reduction in the number of clusters ($\mathcal{R} = 0.9$) leads to speed-up factors of 3 and 215 compared to $\mathcal{R} = 0$ and DC respectively. In the 2-D FGM calculations, a speed-up of 4.5 is achieved for an increase in the clustering factor from $\mathcal{R} = 0$ to $\mathcal{R} = 0.9$.

Understandably, the extensive computational speed-up is primarily the consequence of a drastic reduction in the number of transport equations needed to be solved for the gas-phase species (through FGM) and sectional soot mass fractions (through clustering). In addition, the tabulation of the soot source terms avoids the computationally intensive calculation of the soot particle dynamics (coagulation process). Although the impact of clustering on the overall speed-up is somewhat moderate compared to the use of FGM, it facilitates a significant reduction in the memory consumption of the FGM database and post-processed variables. Therefore, the FGM-CDSM approach tends to deliver a drastic advantage in terms of the memory footprint of the CFD simulations besides the aforementioned reduction in computational cost.

6. Conclusions

A computationally efficient strategy to predict the formation of soot and the evolution of its PSDF is proposed by integrating the discrete sectional method-based soot model with Flamelet Generated Manifold chemistry and is referred to as FGM-CDSM. The FGM-CDSM comprises clustering of soot sections to enable the low dimensional description of PSDF and minimize the computational cost. In this work, FGM-CDSM is applied to simulations of laminar non-premixed flames for the assessment of its accuracy and computational performance against a detailed kinetics-based sectional soot model.

Numerical results revealed that the FGM-CDSM tends to reproduce the global soot quantities and their dynamic response captured by detailed kinetics reasonably well. Moreover, the introduction of clustering demonstrated a minimal effect on the overall accuracy of soot prediction, apart from slight discrepancies in quantitative prediction. Computational performance analysis indicated that the application of FGM-CDSM facilitates the reduction of CPU time by approximately two orders of magnitude compared to the detailed chemistry-based simulations.

Although the assumption of soot following its steady flamelet behavior may not have physical evidence, the current study

demonstrates it to be a reasonably good approximation to reproduce the soot formation in steady and unsteady conditions while proposing an efficient modeling strategy (clustering) for sooting flame simulations. The results presented here show certain limitations of the model to capture accurately the soot formation during the onset and early stages of the soot process. In fact, when information on soot evolution from the gas phase to the steady state is not included in the manifold, the model's performance is affected. However, this issue is primarily related to the flamelet generation rather than the tabulated soot chemistry or the clustering strategy. In this context, the development of a consistent relaxation model for soot source terms, and effective treatment of the chemical history of soot formation in the manifold can be of interest towards application to multidimensional unsteady flames. Finally, it was shown that the accuracy of FGM-CDSM is found to be impacted by clustering distribution. Therefore, further improvements can be sought to establish a more sophisticated distribution of sections in clustering.

In conclusion, the good predictive accuracy, decent computational efficiency along with low memory footprint, make the FGM-CDSM approach a promising candidate for large-scale simulations of turbulent sooting flames. However, further research is required to investigate the performance of FGM-CDSM under turbulent conditions and this is left for future work.

Declaration of Competing Interest

The authors declare that they have no known competing financial interests or personal relationships that could have appeared to influence the work reported in this paper.

Acknowledgments

The research leading to these results has received funding from the European Union's Horizon 2020 Programme under the ESTiMatE project, grant agreement no. 821418. The authors gratefully acknowledge the Red Española de Supercomputación (RES) for computational resources.

Appendix A. Comparison of FGM-CDSM against run-time source term computation strategy

The main objective of the present work is to introduce a computationally efficient FGM-DSM coupling through the tabulation of soot source terms followed by the clustering of soot sections. The limited capability of this method in capturing the chemical history effects of soot formation is evident from the discussion of the results presented here. Hence, it is interesting to illustrate the differences between run-time source term computation and source term tabulation (FGM-CDSM) in predicting soot history effects. The FGM-DSM coupling approach involving run-time soot source term computation has been introduced in our earlier work [16] under the term FGM-Full method. In the FGM-Full method, the sectional soot source terms are computed during the simulation run by using tabulated gas-phase species mass fractions and thermochemical parameters relevant to the soot model.

A test counterflow flame configuration (introduced in Section 3.3.2) describing the unsteady evolution of soot from the pure gas-phase initial solution toward the steady solution is retained for this comparative assessment. The instantaneous profiles of soot volume fraction are compared for FGM-Full and FGM-CDSM ($\mathcal{R} = 0$) in Fig. A.18. As can be noticed, the profiles of soot volume fraction obtained from DC are well reproduced with the FGM-Full strategy. Such a favorable unsteady response of FGM-Full can be attributed to the fact that the separation of soot formation and gas-phase chemistry time scales (with the former being much slower than the latter) is effectively achieved during soot source term computation, as opposed to their tabulation from steady-state flamelets.

The comparison of FGM-CDSM and FGM-Full strategies for unsteady flames with oscillating strain rates (introduced in

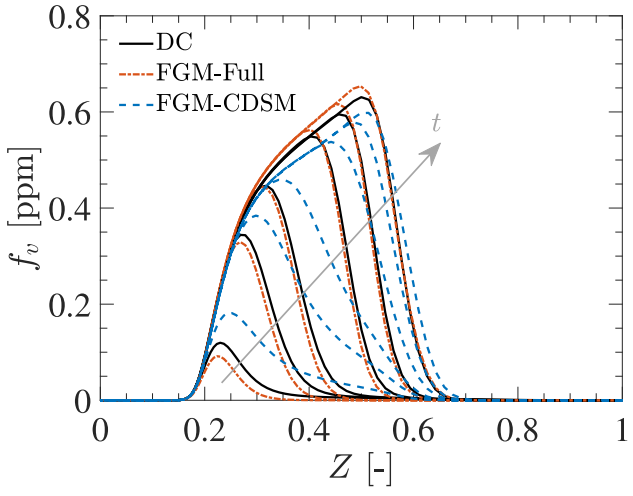

Fig. A.18. Profiles of unsteady evolution of f_v from steady gas-phase solution for DC, FGM-CDSM (no-clustering $\mathcal{R} = 0$), and FGM-Full approaches. The gray arrow indicates time t = 0.5, 1.5, 2.5, 5, 7.5, 12.5 ms.

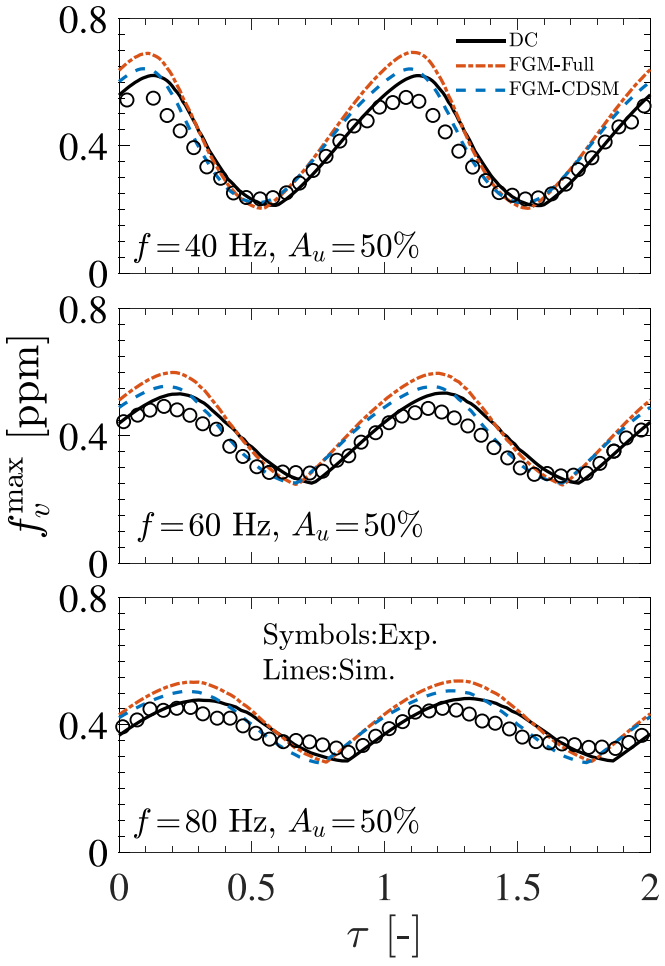

Fig. A.19. Comparison between DC, FGM-CDSM (no-clustering), and FGM-Full solutions for transient evolution of peak soot volume fraction.

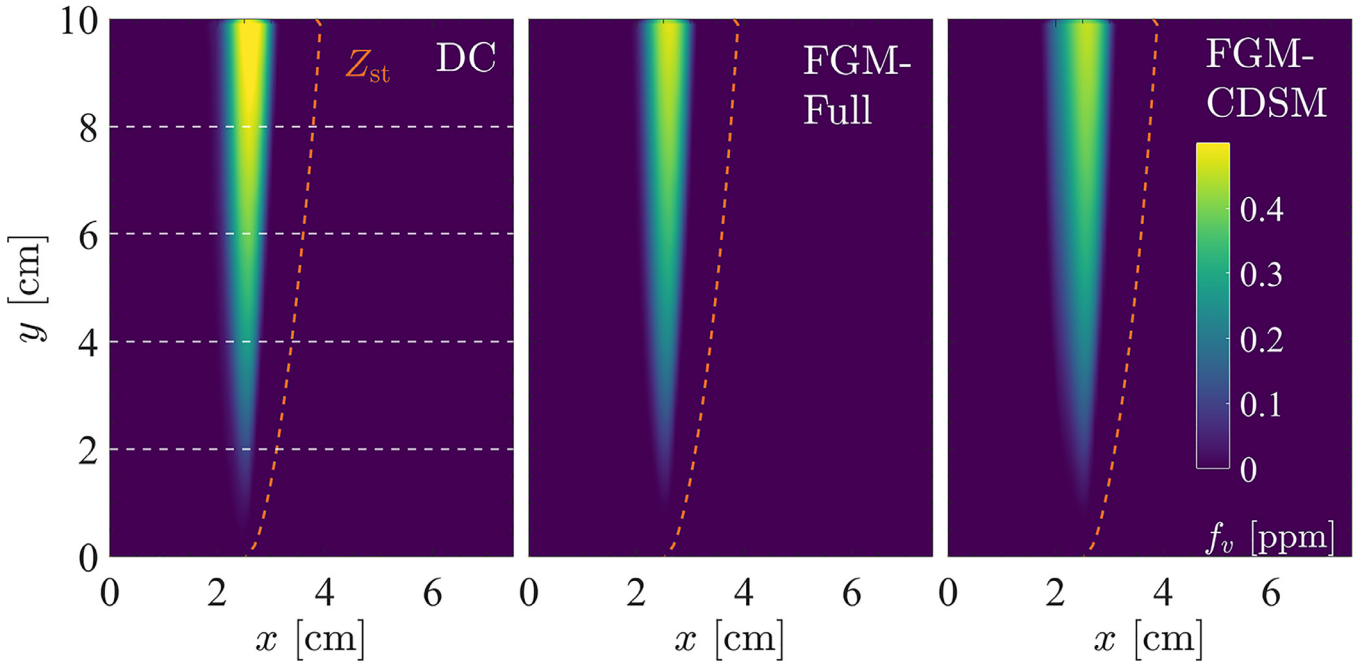

Fig. A.20. Comparison between DC, FGM-CDSM (no-clustering), and FGM-Full solutions for soot volume fraction fields.

Section 3.3.1) is presented in Fig. A.19 for different frequencies. It can be observed that the dynamic response of peak soot volume fraction predicted by FGM-Full, shows a close agreement with DC in terms of phase difference as compared to FGM-CDSM. Since the intra-sectional dependence of soot source terms on soot variables is included in the FGM-Full method, the chemical time scales of soot formation are favorably captured in the FGM-Full method. On the other hand, FGM-CDSM follows the chemical time scales of soot formation based on the tabulated source terms, which are strongly correlated to the dynamic evolution of the progress variable along with soot transport. Despite slight discrepancies when compared with FGM-Full, the accuracy of FGM-CDSM in capturing dynamic responses of soot is encouraging, considering several assumptions surrounding its formulation.

The 2-D laminar configuration introduced earlier (in Section 4) is essentially very similar to this 1-D time-dependent case where unsteady soot evolution is translated into streamwise spatial evolution. In Fig. A.20, the steady-state soot volume fraction fields obtained with DC are compared against FGM-CDSM (with $\mathcal{R} = 0$) and FGM-Full solutions. It can be observed that the distribution of f_v within fuel-rich regions is somewhat better reproduced with the FGM-Full method as compared to the FGM-CDSM method. For a more quantitative illustration, the f_v profiles and PSD (at the peak f_v) obtained with the FGM-Full and FGM-CDSM methods at several downstream positions are compared against their DC counterparts in Fig. A.21. Compared to FGM-CDSM, the f_v profiles in composition space, as well as PSDs, predicted by the FGM-Full approach show good qualitative agreement with DC solutions. Moreover, the diffusion of soot noticed in the fuel-rich region for the FGM-CDSM case is prevented in the FGM-Full approach, as the chemical trajectories of soot formation from the gas phase are captured well in the latter approach. From the comparison between soot prediction with the FGM-CDSM and FGM-Full methods, it is evident that the use of tabulated soot chemistry from steady flamelets for an essentially unsteady soot formation process will not be very accurate. An alternative approach for FGM-CDSM can be suggested to isolate time scales associated with different subprocesses which involve run-time computation for the coagulation process in conjunction with a priori-tabulation of source terms of other soot subprocesses. However, the computational speed-up gained with this approach will be very marginal compared to the FGM-Full method. The calculation of the 2-D coflow flame showed that compared to the run-time computation of the soot source term (FGM-Full), the use of FGM-CDSM yields a speed-up of about 14 (from 40 sections). This speed-up can be further increased by a factor of 60 approximately through the clustering level $\mathcal{R} = 0.9$. The present approach is therefore very useful in the context of the simulation of practical systems.

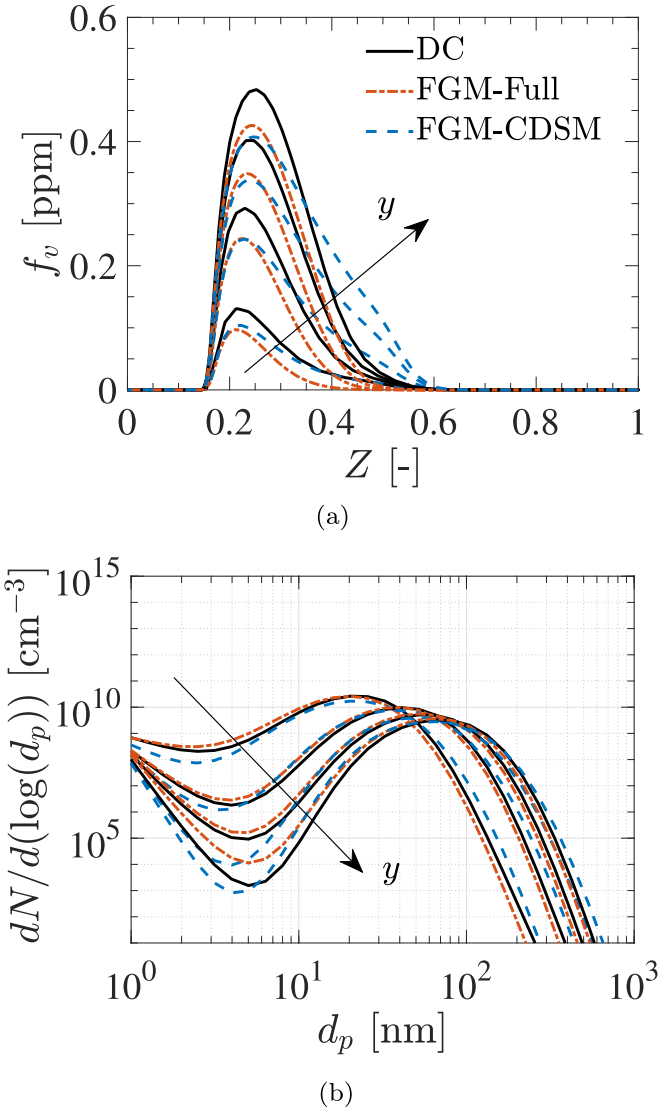

Fig. A.21. Comparison between DC, FGM-CDSM (no-clustering) and FGM-Full solutions for profiles of f_v (a), and PSDF (at $f_v^{\max}$) along $y = 2$, 4, 6, 8 cm downstream positions (b).

References

[1] F. Gelbard, Y. Tambour, J. Seinfeld, Sectional representations for simulating aerosol dynamics, J. Colloid Interface Sci. 76 (2) (1980) 541–556.

[2] K. Netzell, H. Lehtiniemi, F. Mauss, Calculating the soot particle size distribution function in turbulent diffusion flames using a sectional method, Proc. Combust. Inst. 31 (1) (2007) 667–674.

[3] P. Rodrigues, B. Franzelli, R. Vicquelin, O. Gicquel, N. Darabiha, Coupling an LES approach and a soot sectional model for the study of sooting turbulent non-premixed flames, Combust. Flame 190 (2018) 477–499.

[4] C. Hoerlle, F. Pereira, Effects of CO_2 addition on soot formation of ethylene non-premixed flames under oxygen enriched atmospheres, Combust. Flame 203 (2019) 407–423.

[5] M. Frenklach, Method of moments with interpolative closure, Chem. Eng. Sci. 57 (12) (2002) 2229–2239.

[6] M. Mueller, G. Blanquart, H. Pitsch, Hybrid method of moments for modeling soot formation and growth, Combust. Flame 156 (6) (2009) 1143–1155.

[7] S. Salenbauch, A. Cuoci, A. Frassoldati, C. Saggese, T. Faravelli, C. Hasse, Modeling soot formation in premixed flames using an extended conditional quadrature method of moments, Combust. Flame 162 (6) (2015) 2529–2543.

[8] P. Mitchell, M. Frenklach, Monte Carlo simulation of soot aggregation with simultaneous surface growth-why primary particles appear spherical, Proc. Combust. Inst. 27 (1) (1998) 1507–1514.

[9] M. Balthasar, M. Kraft, A stochastic approach to calculate the particle size distribution function of soot particles in laminar premixed flames, Combust. Flame 133 (3) (2003) 289–298.

[10] M. Mueller, H. Pitsch, LES model for sooting turbulent nonpremixed flames, Combust. Flame 159 (6) (2012) 2166–2180.

[11] S. Yang, J. Lew, M. Mueller, Large eddy simulation of soot evolution in turbulent reacting flows: presumed subfilter PDF model for soot–turbulence–chemistry interactions, Combust. Flame 209 (2019) 200–213.

[12] H. Colmán, A. Cuoci, N. Darabiha, B. Fiorina, A virtual chemistry model for soot prediction in flames including radiative heat transfer, Combust. Flame 238 (2022) 111879.

[13] M. Jadidi, S. Kostic, L. Zimmer, S.B. Dworkin, An artificial neural network for the low-cost prediction of soot emissions, Energies 13 (18) (2020) 4787.

[14] Y. Xuan, G. Blanquart, Effects of aromatic chemistry-turbulence interactions on soot formation in a turbulent non-premixed flame, Proc. Combust. Inst. 35 (2) (2015) 1911–1919.

[15] D. Aubagnac-Karkar, J. Michel, O. Colin, P. Vervisch-Kljakic, N. Darabiha, Sectional soot model coupled to tabulated chemistry for diesel RANS simulations, Combust. Flame 162 (8) (2015) 3081–3099.

[16] A. Kalbhor, J. van Oijen, An assessment of the sectional soot model and FGM tabulated chemistry coupling in laminar flame simulations, Combust. Flame 229 (2021) 111381.

[17] D. Carbonell, A. Oliva, C.D. Perez-Segarra, Implementation of two-equation soot flamelet models for laminar diffusion flames, Combust. Flame 156 (3) (2009) 621–632.

[18] L. Zimmer, Numerical Study of soot Formation in Laminar Ethylene Diffusion Flames, Universidade Federal do Rio Grande do Sul, Porto Alegre, Brazil, 2016 Ph.D. thesis.

[19] H. Bao, A. Kalbhor, N. Maes, B. Somers, J. van Oijen, Investigation of soot formation in n-dodecane spray flames using LES and a discrete sectional method, Proc. Combust. Inst. (2022), doi:10.1016/j.proci.2022.07.089.

[20] J. van Oijen, L. de Goey, Modelling of premixed laminar flames using flamelet–generated manifolds, Combust. Sci. Technol. 161 (1) (2000) 113–137.

[21] J. van Oijen, A. Donini, R. Bastiaans, J. ten Thije Boonkkamp, L. de Goey, State-of-the-art in premixed combustion modeling using flamelet generated manifolds, Prog. Energy Combust. Sci. 57 (2016) 30–74.

[22] N. Peters, Laminar flamelet concepts in turbulent combustion, Proc. Combust. Inst. 21 (1) (1988) 1231–1250.

[23] M. Frenklach, H. Wang, Detailed modeling of soot particle nucleation and growth, Proc. Combust. Inst. 23 (1) (1991) 1559–1566.

[24] J. Appel, H. Bockhorn, M. Frenklach, Kinetic modeling of soot formation with detailed chemistry and physics: laminar premixed flames of C2 hydrocarbons, Combust. Flame 121 (1–2) (2000) 122–136.

[25] S. Kumar, D. Ramkrishna, On the solution of population balance equations by discretization—I. A fixed pivot technique, Chem. Eng. Sci. 51 (8) (1996) 1311–1332.

[26] A. Kalbhor, J. van Oijen, Effects of hydrogen enrichment and water vapour dilution on soot formation in laminar ethylene counterflow flames, Int. J. Hydrogen Energy 45 (43) (2020) 23653–23673.

[27] A. Wick, A. Attili, F. Bisetti, H. Pitsch, DNS-driven analysis of the flamelet/progress variable model assumptions on soot inception, growth, and oxidation in turbulent flames, Combust. Flame 214 (2020) 437–449.

[28] Y. Xuan, G. Blanquart, A flamelet-based a priori analysis on the chemistry tabulation of polycyclic aromatic hydrocarbons in non-premixed flames, Combust. Flame 161 (6) (2014) 1516–1525.

[29] L. Somers, The Simulation of Flat Flames with Detailed and Reduced Chemical Models, Eindhoven University of Technology, Eindhoven, the Netherlands, 1994 Ph.D. thesis.

[30] C. Hoerlle, Modelling of Soot Formation Based on the Discrete Sectional Method: CO_2 Effects and Coupling with the FGM Technique, Universidade Federal do Rio Grande do Sul, Porto Alegre, Brazil, 2020 Ph.D. thesis.

[31] Y. Wang, A. Raj, S. Chung, A PAH growth mechanism and synergistic effect on PAH formation in counterflow diffusion flames, Combust. Flame 160 (9) (2013) 1667–1676.

[32] J. Hirschfelder, C. Curtiss, R. Bird, Molecular Theory of Gases and Liquids, second ed., John Wiley and Sons, Inc., New York, NY, 1964.

[33] R. Bilger, S. Stårner, R. Kee, On reduced mechanisms for methane-air combustion in nonpremixed flames, Combust. Flame 80 (2) (1990) 135–149.

[34] Y. Wang, A. Raj, S. Chung, Soot modeling of counterflow diffusion flames of ethylene-based binary mixture fuels, Combust. Flame 162 (3) (2015) 586–596.

[35] Y. Wang, S. Chung, Formation of soot in counterflow diffusion flames with carbon dioxide dilution, Combust. Sci. Technol. 188 (4–5) (2016) 805–817.

[36] L. Xu, F. Yan, M. Zhou, Y. Wang, S. Chung, Experimental and soot modeling studies of ethylene counterflow diffusion flames: non-monotonic influence of the oxidizer composition on soot formation, Combust. Flame 197 (2018) 304–318.

[37] A. Kalbhor, J. van Oijen, Effects of curvature on soot formation in steady and unsteady counterflow diffusion flames, Combust. Flame 241 (2022) 112108.

[38] A. Cuoci, A. Frassoldati, T. Faravelli, E. Ranzi, Formation of soot and nitrogen oxides in unsteady counterflow diffusion flames, Combust. Flame 156 (10) (2009) 2010–2022.

[39] A. Cuoci, A. Frassoldati, T. Faravelli, E. Ranzi, Soot formation in unsteady counterflow diffusion flames, Proc. Combust. Inst. 32 (1) (2009) 1335–1342.

[40] P. Rodrigues, B. Franzelli, R. Vicquelin, O. Gicquel, N. Darabiha, Unsteady dynamics of PAH and soot particles in laminar counterflow diffusion flames, Proc. Combust. Inst. 36 (1) (2017) 927–934.

[41] G. Li, M. Zhou, Y. Wang, Sensitivity of soot formation to strain rate in steady counterflow flames determines its response under unsteady conditions, Combust. Flame 241 (2022) 112107.

[42] S. Delhaye, L. Somers, J. van Oijen, L. de Goey, Incorporating unsteady flow–effects in flamelet-generated manifolds, Combust. Flame 155 (1–2) (2008) 133–144.
[43] H. Pitsch, M. Ihme, An unsteady/flamelet progress variable method for LES of nonpremixed turbulent combustion, 43rd AIAA Aerospace Sciences Meeting and Exhibit (2005), p. 557.
[44] M. Vázquez, G. Houzeaux, S. Koric, A. Artigues, J. Aguado-Sierra, R. Arís, D. Mira, H. Calmet, F. Cucchietti, H. Owen, et al., Alya: multiphysics engineering simulation toward exascale, J. Comput. Sci. 14 (2016) 15–27.
[45] D. Mira, O. Lehmkuhl, A. Both, P. Stathopoulos, T. Tanneberger, T.G. Reichel, C.O. Paschereit, M. Vázquez, G. Houzeaux, Numerical characterization of a premixed hydrogen flame under conditions close to flashback, Flow, Turbul. Combust. 104 (2) (2020) 479–507.
[46] A. Both, O. Lehmkuhl, D. Mira, M. Ortega, Low-dissipation finite element strategy for low mach number reacting flows, Comput. Fluids 200 (2020) 104436.
[47] S. Gövert, D. Mira, J. Kok, M. Vázquez, G. Houzeaux, The effect of partial premixing and heat loss on the reacting flow field prediction of a swirl stabilized gas turbine model combustor, Flow, Turbul. Combust. 100 (2) (2018) 503–534.
[48] H. Guo, G. Smallwood, The effect of preferential diffusion on soot formation in a laminar ethylene/air diffusion flame, Combust. Theor. Model. 15 (1) (2010) 125–140.
[49] N. Malik, T. Løvås, F. Mauss, The effect of preferential diffusion on the soot initiation process in ethylene diffusion flames, Flow, Turbul. Combust. 87 (2) (2011) 293–312.